Geochemistry, Geophysics, Geosystems

RESEARCH ARTICLE
10.1029/2017GC007394

The Low-Temperature Besnus Magnetic Transition: Signals Due to Monoclinic and Hexagonal Pyrrhotite

Chorng-Shern Horng[1] and **Andrew P. Roberts**[2]

[1]Institute of Earth Sciences, Academia Sinica, Nangang, Taipei, Taiwan, [2]Research School of Earth Sciences, Australian National University, Canberra, ACT, Australia

This article is a companion to Horng (2018) https://doi.org/10.1002/2017JB015262.

Key Points:
- Monoclinic pyrrhotite is observed consistently to record a Besnus transition at ~30–34 K
- Hexagonal 3T pyrrhotite does not record a Besnus transition, but it has previously unknown room- and low-temperature remanent magnetizations
- The 3T pyrrhotite is common in gas hydrate/methane venting areas, so a more detailed understanding of its magnetic properties is needed

Correspondence to:
C.-S. Horng,
cshorng@earth.sinica.edu.tw

Citation:
Horng, C.-S., & Roberts, A. P. (2018). The low-temperature Besnus magnetic transition: Signals due to monoclinic and hexagonal pyrrhotite. *Geochemistry, Geophysics, Geosystems*, *19*, 3364–3375. https://doi.org/10.1029/2017GC007394

Received 11 DEC 2017
Accepted 4 JUN 2018
Accepted article online 19 JUN 2018
Published online 23 SEP 2018

Abstract The low-temperature magnetic properties of the many pyrrhotite varieties have not been studied extensively. Monoclinic pyrrhotite (Fe_7S_8) goes through the Besnus transition at ~30–34 K, which is used widely to diagnose its presence in bulk samples. Other pyrrhotite polytypes are assumed to be antiferromagnetic, although it has been suggested occasionally that some may also have remanence-carrying capabilities. Here we compare the magnetic properties of monoclinic (4M) and hexagonal (3T) pyrrhotite at low temperatures. The 4M pyrrhotite records a Besnus transition consistently. Despite not recording a Besnus transition, 3T pyrrhotite has a magnetic remanence at room temperature and has distinctive room- and low-temperature magnetic properties that cannot be explained by known or unidentified impurities (with abundances $<$0.1%). Some 3T-pyrrhotite samples have exceptionally high ($>$700 mT) and stable coercivities below 50 K. The importance of this mineral in fossil or active gas hydrate and methane venting environments makes it important to develop a more detailed understanding of its occurrences and magnetic properties.

1. Introduction

Pyrrhotite ($Fe_{1-x}S$, x = 0–0.125) has variable crystal structures, Fe/S contents, and magnetic properties. At ambient temperatures, monoclinic pyrrhotite (Fe_7S_8) is ferrimagnetic, while more S-rich compositions (Fe_9S_{10}, $Fe_{11}S_{12}$) are antiferromagnetic (O'Reilly et al., 2000; Pósfai et al., 2000). Smythite (Fe_9S_{11}) does not have a Fe/S ratio that fits the above definition for pyrrhotite, but it has a similar crystal structure as monoclinic pyrrhotite and is ferrimagnetic at ambient temperatures (Hoffmann et al., 1993). Hexagonal pyrrhotite (Fe_9S_{10}) is antiferromagnetic at ambient temperatures and becomes ferrimagnetic at the so-called γ transition at 200–220 °C, and ferrimagnetic ordering is preserved up to its Curie temperature at 275–295 °C (Rochette, 1987; Rochette et al., 1990; Schwarz, 1975). Upon cooling back through the γ transition to room temperature, hexagonal pyrrhotite remains a metastable ferrimagnet (Bennett & Graham, 1981).

A low-temperature magnetic transition has been reported for monoclinic pyrrhotite (Besnus & Meyer, 1964; Dekkers et al., 1989; Fillion & Rochette, 1988; Rochette et al., 1990). Its origin has not been studied extensively. This magnetic transition was originally suggested to have a similar origin to the Verwey transition in magnetite (Besnus & Meyer, 1964; Fillion & Rochette, 1988). The Verwey transition (Verwey, 1939) results from a crystallographic change from cubic above the transition temperature to monoclinic below it and is accompanied by an order of magnitude change in magnetocrystalline anisotropy that controls the magnetic property change across the transition (e.g., Walz, 2002). No crystallographic change was detected in monoclinic pyrrhotite across its low-temperature transition from neutron powder diffraction analysis (Powell et al., 2004), whereas based on detailed single crystal neutron diffraction analyses and anisotropy measurements across the transition, Wolfers et al. (2011) proposed that the room temperature monoclinic structure transforms into a low-temperature triclinic structure due to distortion of the shape of Fe octahedra. A shift in the direction of the easy axis of magnetization by about $\pm\pi/4$ occurs below the transition (Wolfers et al., 2011). In contrast, Koulialias et al. (2016) suggested that the low-temperature transition in pyrrhotite is due to stronger antiferromagnetic coupling between different monoclinic magnetic superstructures (4C and 5C*) below the transition temperature that form a single anisotropy system with higher magnetization and coercivity than above the transition. Volk et al. (2016) measured the angular dependence of magnetic properties in the basal plane of monoclinic pyrrhotite and reported a change from a fourfold symmetry above to sixfold symmetry below the Besnus transition with inflections in hysteresis loops that they attributed to field and temperature-dependent easy axis switching. They concluded that these changes are most likely due to a crystallographic change from a monoclinic to triclinic structure below the transition, in support of the conclusion of Wolfers et al. (2011).

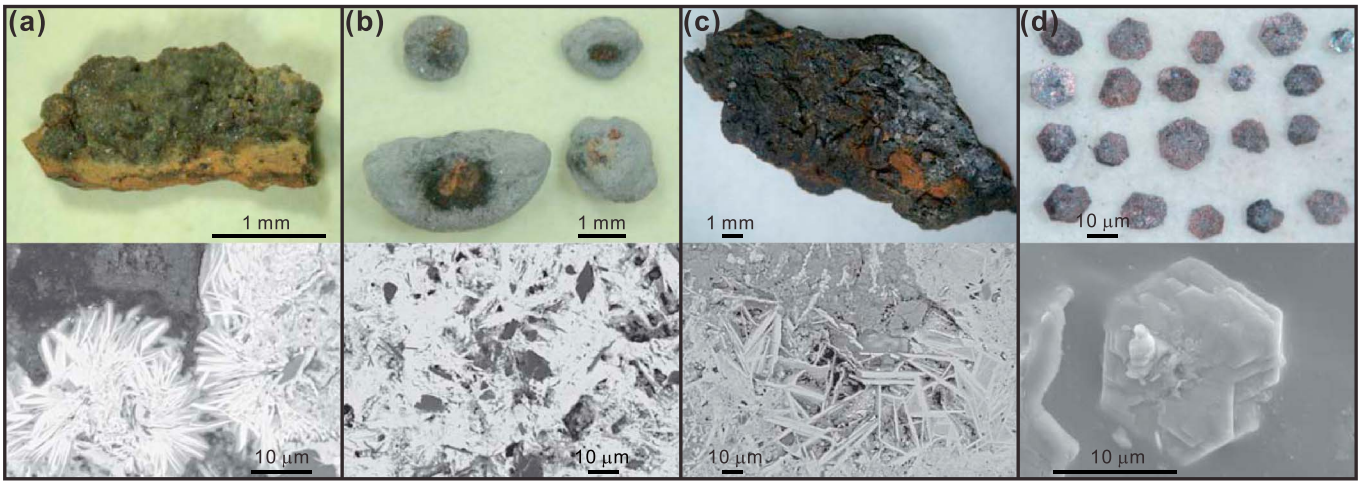

Figure 1. Paired optical and scanning electron microscope images of the studied pyrrhotite-bearing samples. (a) Authigenic pyrrhotite nodule from a depth of 7.22 m in marine sediment core MD10-3276 from a gas hydrate area offshore of southwestern Taiwan with surficial crust consisting mainly of goethite. Numerous authigenic pyrrhotite nodules were also found at other depths (e.g., 4.90 m, 11.42 m, and 12.02 m). The electron back-scattered SEM image reveals interlocking ~10-μm plates of hexagonal (3T) pyrrhotite (Horng, 2018). (b) Four authigenic pyrrhotite nodules from tectonically uplifted Plio-Pleistocene marine sediments from a fossil gas hydrate zone (Erh-Jen Chi, EJC, section, site 29; Jiang et al., 2001), southwestern Taiwan. The gray material around the nodules in the upper image is the mudstone that hosts the nodule. The SEM image reveals interlocking ~10- to 20-μm hexagonal (3T) pyrrhotite plates. (c) Authigenic pyrrhotite nodule from tectonically uplifted Plio-Pleistocene marine sediments from the Valle Ricca section, near Rome, Italy (Florindo & Sagnotti, 1995), which is also a fossil gas hydrate zone (van Dongen et al., 2007). The SEM image reveals interlocking ~30- to 40-μm plates of hexagonal (3T) pyrrhotite (bright) with goethite that has filled spaces between plates. Greigite is also present in this sample. (d) Upper: Reflected light image of ~10- to 20-μm pseudohexagonal monoclinic (4M) detrital pyrrhotite grains extracted from the core catcher of marine sediment core MD10-3292, which were eroded from metamorphic terrains in Taiwan (Horng et al., 2012). Lower: SEM image of one such grain. SEM = scanning electron microscope.

Monoclinic pyrrhotite is generally considered to be the paleomagnetically most significant pyrrhotite polytype even though the same Fe/S ratio can be produced by variable Fe site occupation and variable crystallographic *c* axis dimension (Pósfai et al., 2000). Thus, when a magnetic remanence-bearing pyrrhotite is detected in geological studies, it is usually assumed to be monoclinic (Horng & Roberts, 2006; Kars & Kodama, 2015; Larrasoaña et al., 2007; Roberts, 2015). In contrast, the paleomagnetic signal of Martian meteorites has been attributed to hexagonal pyrrhotite in a metastable ferromagnetic form (cf. Bennett & Graham, 1981) caused by either shock, quenching, or irradiation damage (Rochette et al., 2005). Given the variable composition of pyrrhotite and Fe site occupancy, it is reasonable to question whether remanence-bearing properties exist in different pyrrhotite polytypes over various temperature ranges. For example, Rochette et al. (1990) reported anomalous magnetic properties, including high coercivities, of some pyrrhotite samples at low temperatures compared to typical results for monoclinic pyrrhotite even though the samples recorded a Besnus transition. They suggested, based on the variable stoichiometry and magnetic superstructures in pyrrhotite, that such samples could represent a different type of remanence-bearing pyrrhotite. Few detailed magnetic property studies of various pyrrhotite polytypes have been undertaken to assess such possibilities.

In this study, we present low-temperature magnetic results for mineralogically well-characterized monoclinic and hexagonal pyrrhotite samples to document the poorly known low-temperature magnetic properties of hexagonal pyrrhotite by comparison with monoclinic pyrrhotite. We also assess the assumption that monoclinic pyrrhotite is the main pyrrhotite species that can carry a remanent magnetization at paleomagnetically important ambient temperatures.

2. Samples and Methods

Authigenic hexagonal pyrrhotite-bearing nodules were obtained from several sources (Figures 1a–1c). They include: marine sediment core MD10-3276 from an active gas hydrate area offshore of southwestern Taiwan (Horng, 2018), tectonically uplifted Plio-Pleistocene marine sediments from the Erh-Jen Chi (EJC) mudstone section, southwestern Taiwan (Jiang et al., 2001), and tectonically uplifted Plio-Pleistocene marine mudstones from Valle Ricca, near Rome, Italy (Florindo & Sagnotti, 1995; van Dongen et al., 2007). The latter two settings

are fossil gas hydrate zones. Monoclinic pyrrhotite grains are from a phyllite from the M11 metamorphic section, Taiwan Central Range (Horng et al., 2012). Such grains are also abundant in marine sediments offshore of Taiwan, which were eroded from metamorphic terrains and transported by rivers to the sea (Figure 1d). Bulk phyllite and magnetic extracts were analyzed here; extracts were obtained by crushing the rock into a powder and extracting pyrrhotite with a rare-earth magnet from a slurry, with repeated magnetic purification. A small portion was used to obtain X-ray diffraction (XRD) patterns for crystal structure analysis. The rest of the sample was subdivided into five size fractions (63–125, 20–38, 10–20, 2–10, and < 2 μm) with sieves and membrane filters. Results for these samples are supplemented by analyses of monoclinic pyrrhotite from ore-grade sulfide deposits and museum samples (crystal fragments), and detrital pyrrhotite extracted from sediments from the core catcher of marine core MD10-3292 (Figure 1d).

XRD analysis was performed after powdering samples to sizes <10 μm, to identify mineral components using a Wiggler X-ray beamline (BL17A1) at the National Synchrotron Radiation Research Center, Taiwan (wavelength $\lambda = 1.32090$ Å). Synchrotron-based XRD analysis provides several important advantages over conventional laboratory-based analyses. The intensity of a synchrotron X-ray beam is 10^6 times higher than standard laboratory systems, which means that analyses are rapid (several minutes), peaks are sharper and better resolved with less overlap with neighboring peaks because of the use of an area detector rather than a point detector, and better signal to noise ratios are obtained so that minerals with concentrations $<0.1\%$ can be detected (this limit depends on scattering and the crystallinity of the material analyzed). These aspects enable precise identification of potential magnetic impurities within the studied samples. Original 2θ angles ($\lambda = 1.32090$ Å) were converted to those based on conventional Cu Kα radiation ($\lambda = 1.54056$ Å) with background subtraction at lower angles using WinPLOTR software.

To understand textural relationships among the XRD-identified minerals and to assess potential cation substitution within the minerals, petrographic observations were made on polished sections of bulk samples using a JEOL JSM-6360LV scanning electron microscope (SEM) at 15 keV and 18-nA acceleration voltage, with a 10-μm beam diameter. Chemical compositions of sedimentary minerals were determined using an Oxford Instruments Ltd INCA-300 X-ray energy dispersive spectrometer (EDS) attached to the SEM. Chemical compositions of metamorphic pyrrhotite samples were determined using a JEOL JXA-8500F field emission electron probe microanalyzer system with five-channel wavelength dispersive X-ray spectrometers. Quantitative analyses were conducted using beam conditions of 20 kV, 5 nA, and 2 μm for the acceleration voltage, current, and beam diameter, respectively.

Magnetic hysteresis parameters, including saturation remanent magnetization (M_{rs}), saturation magnetization (M_s), coercivity (B_c), and coercivity of remanence (B_{cr}), were measured at room temperature using a Princeton Measurements Corporation vibrating sample magnetometer to maximum fields of ±1.0 T. Samples were weighed with a precision of 0.1 mg and magnetic parameters are expressed in mass-specific terms. Some samples were selected for low-field magnetic susceptibility (χ) measurements of initial slopes at low fields (0–0.03 T) with the slopes of loops corrected at high fields (0.8–1.0 T; see Horng (2018) for details).

Low-temperature magnetic measurements were made on the samples using a Quantum Design superconducting quantum interference device vibrating sample magnetometer. Saturation isothermal remanent magnetization (SIRM) warming experiments were carried out by cooling samples from room temperature to 5 K in zero-field. At 5 K, a 5 T direct current (DC) field was applied and was then switched off to impart a SIRM, which was measured to 300 K at a heating rate of 3 K/min in zero-field. Low-temperature cycling (LTC) of a room temperature SIRM (RT-SIRM) was also measured by imparting a RT-SIRM in a 5-T DC field, switching off and canceling the field, and measuring the SIRM to 5 K and then back to 300 K in zero-field. Rochette et al. (1990) reported that both coercivity (B_c) and RT-SIRM change in a step-like manner during cooling and warming through ~34 K. Hysteresis measurements were also made at low temperatures for the studied samples from which B_c was estimated to investigate whether such changes occur in our samples. Finally, zero-field-cooled (ZFC) and field-cooled (FC) magnetizations were measured during warming from 5 K to room temperature as follows. Samples were first cooled from room temperature to 5 K in zero field. At 5 K, a 5-T DC field was applied and was then switched off to impart a SIRM. SIRM curves were measured to 300 K at a heating rate of 3 K/min. A FC magnetization curve was then measured by applying a 5-T DC field throughout cooling of samples from room temperature to 5 K. At 5 K, the field was switched off to impart a SIRM that was then measured to 300 K at a heating rate of 3 K/min.

3. Results

In all cases, synchrotron XRD analysis provides clear diffraction patterns for detailed mineral identification. Among the authigenic pyrrhotite-bearing nodules (Figures 2a–2c), hexagonal (3T) pyrrhotite is the only polytype that fits the pyrrhotite diffraction patterns shown in Figures 2a–2c, 2e, and 2e-1, which has a single, most intense reflection peak at ~44.03°. Other impurities are present, including quartz, lepidocrocite, pyrite, and elemental S, along with magnetic minerals such as goethite (in all samples) and greigite (Valle Ricca). Instead of the single hexagonal (3T) pyrrhotite peak at ~44.03°, our metamorphic pyrrhotite samples have a split diffraction doublet at ~43.83° and ~44.05° as the most intense pair of peaks (Figures 2d and 2d-1). The metamorphic pyrrhotite is a monoclinic (4M) type. The characteristic single and double peaks are always observed in our sedimentary and metamorphic pyrrhotite samples, respectively, which indicates that they have crystal structures due to hexagonal (3T) and monoclinic (4M) pyrrhotite, respectively (Arnold, 1966; Fleet, 1971; Graham, 1969; Morimoto et al., 1975). The concentration of each identified mineral was determined using Rietveld (1969) refinement (Table 1). In all cases, the total mineral content summed to 100.0% within rounding errors.

The possible presence of other cations within the crystal structure of the studied pyrrhotite samples was assessed using EDS analysis in conjunction with SEM observations for authigenic pyrrhotite samples and using an electron microprobe for monoclinic pyrrhotite samples. The electron beam diameters for these analyses were 10 μm and 2 μm, respectively, where the former size is larger than the minerals analyzed (Figure 3), so all analyses (Table 2) represent composite results. This is evident in the divergence from expected S/Fe ratios of 1.11 and 1.14 for hexagonal (3T) and monoclinic pyrrhotite, respectively. Some of the Fe contributes to iron oxyhydroxides that are identified as oxidation products in the XRD results (Figure 2) and by areas with different electron backscatter in SEM images (Figure 3). For EJC nodule samples, additional Al and Si peaks are identified (Table 2), which are from aluminosilicate matrix minerals. While these results are not mineralogically diagnostic, they enable identification of cations that could be substituted into the pyrrhotite crystal lattice.

None of the analyzed authigenic pyrrhotite nodules from core MD10-3276 and Valle Ricca contain impurity cations. In contrast, some authigenic pyrrhotite nodules from the EJC locality contain trace abundances (tenths of a percent) of As and/or Cu (Table 2). The analyzed metamorphic pyrrhotite samples contain trace abundances of Ni and/or As (0.14–0.23% and 0.02–0.04%, respectively; Table 2). Pyrrhotite has a NiAs structure and both Ni and As are common trace constituents of monoclinic and hexagonal pyrrhotite (e.g., Batt, 1972; Clark, 1960). Cu is also a common metal in pyrrhotite-bearing rocks. While Ni is likely to be incorporated within the crystal structure, pyrite and pyrrhotite are efficient absorbers of As in solution (Han & Fyfe, 2000). With the available analyses, it is not possible to confirm whether the trace As impurities in the authigenic EJC pyrrhotites occur within the crystal structure or whether it is absorbed onto mineral surfaces. These cations have relatively minor concentrations in the EJC samples and are absent in the hexagonal (3T) pyrrhotite nodules from core MD10-3276 and Valle Ricca. Thus, it appears that the documented magnetic properties are due largely to pure authigenic pyrrhotite without cation substitution.

Our focus in this paper is on comparing the low-temperature magnetic properties of hexagonal (3T) and monoclinic pyrrhotite, and we do not report high-temperature data. Horng (2018) presented thermomagnetic curves for a monoclinic pyrrhotite and a representative authigenic pyrrhotite nodule from core MD10-3276. The monoclinic pyrrhotite sample has a reversible thermomagnetic curve with Curie temperature at the expected value of 325 °C (Dekkers, 1989a). The hexagonal (3T) pyrrhotite sample has an irreversible thermomagnetic curve, with thermal alteration appearing to start above ~200 °C. The cooling curve has an upward inflection below 300 °C, which is likely to represent the γ transition in hexagonal pyrrhotite (Bennett & Graham, 1981; Rochette et al., 1990; Schwarz, 1975). The fact that the magnetization after completion of the heating-cooling cycle is the same as before heating (Horng, 2018) indicates that the hexagonal pyrrhotite has undergone quenching and has retained the high-temperature ferrimagnetic phase (Bennett & Graham, 1981). Importantly, the thermomagnetic results of Horng (2018) for hexagonal (3T) pyrrhotite help to rule out significant impurity remanences. Greigite also has thermomagnetic properties that are governed by thermal alteration at similar temperatures (Roberts et al., 2011), but the presence of greigite is ruled out by synchrotron XRD results for this sample (Horng, 2018).

Low-temperature magnetic properties (Figures 4 and 5) for the studied samples differ according to the crystal structure differences (hexagonal and monoclinic) identified from XRD results (Figure 2). Monoclinic pyrrhotite

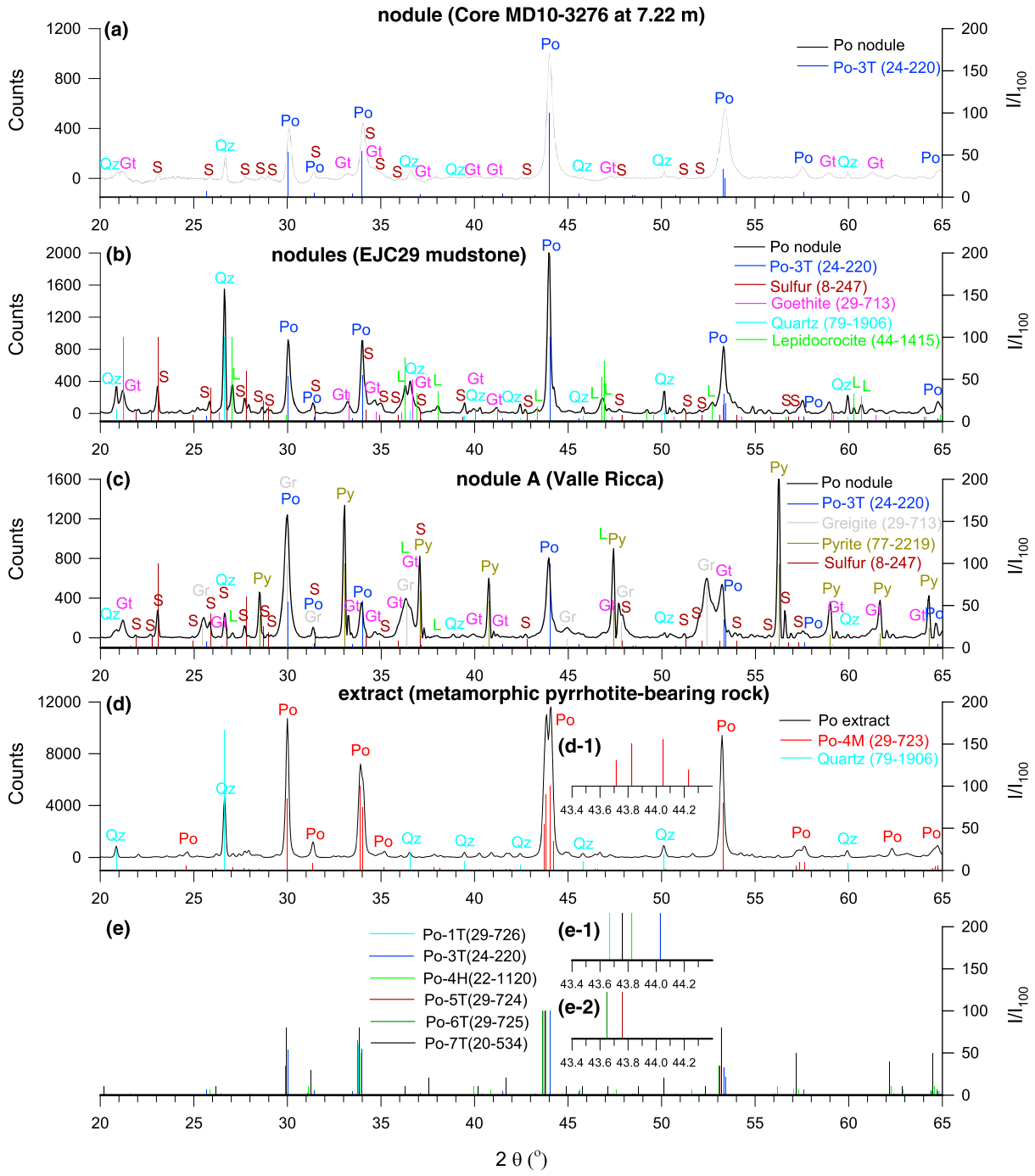

Figure 2. Representative X-ray diffractograms for (a–d) the four samples shown in Figure 1, and (d–1 and e) reference spectra from the respective powder diffraction files (PDFs) for six hexagonal (1T, 3T, 4H, 5T, 6T, 7T) pyrrhotite polytypes and monoclinic (4M) pyrrhotite from the International Centre for Diffraction Data (ICDD; Mineral Powder Diffraction File Databook, 1993). PDF numbers for the pyrrhotite (Po) polytypes are as follows: #29–726 (Po-1T), #24–220 (Po-3T), #22–1120 (Po-4H), #29–724 (Po-5T), #29–725 (Po-6T), #20–534 (Po-7T), and #29–723 (Po-4M). The samples contain various impurities (Py: pyrite; S: sulfur; Gt: goethite; Gr: greigite; L: lepidocrocite; and Qz: quartz), which are indicated by labels beside peaks. PDF numbers (#) of these minerals are: #71–2219 (Py), #8–247 (S), #29–713 (Gt), #16–713 (Gr), #44–1415 (L), and #79–1906 (Qz); their diffraction positions and relative intensities are shown with vertical lines with respect to the largest peak (I/I_{100}), respectively. Based on these results, the authigenic pyrrhotite is always hexagonal (3T) and the metamorphic pyrrhotite is monoclinic (4M).

Table 1
Mineral Concentration Estimates for Studied Samples From Refinement of XRD Results

Sample	Pyrrhotite 3T (%)	Pyrrhotite 4M (%)	Pyrite (%)	Greigite (%)	Sulfur (%)	Quartz (%)	Goethite (%)	Lepidocrocite (%)	Total (%)
MD3276 4.9 m	43.27		49.85		0.88	1.15	4.85		100.00
MD3276 7.22 m	64.80				12.76	5.07	17.38		100.01
MD3276 11.42 m	69.00				6.70	1.68	22.62		100.00
MD3276 12.02 m	18.09		4.69		26.91	2.50	47.82		100.01
EJC29 Nodules	44.48				10.25	17.12	18.40	9.75	100.00
Valle Ricca Nodule A	20.89		18.35	40.26	6.72	2.01	10.68	1.09	100.00
M11–131 Po extract		89.85				10.15			100.00

in the studied bulk metamorphic rocks, magnetic extracts from metamorphic rocks and marine sediments, and crystal fragments from museum specimens and hydrothermal ore deposits, always gives rise to a sharp Besnus transition in SIRM warming curves (Figure 4a) and ZFC/FC curves (Figure 5a). The sharpness of the transition is clear from the first derivative of the SIRM warming curves (Figure 4b). In contrast, the sedimentary authigenic hexagonal pyrrhotite-bearing nodules have no low-temperature transition (Figures 4c, 4d, and 5b). It is important to note that while most of the pyrrhotites appear to be pure iron sulfides, the sedimentary nodule samples contain other minerals (Figures 2a–2c), so the observed low-temperature magnetic properties could have contributions due to trace impurities. The results contain no Verwey or Morin transitions due to magnetite or hematite, respectively (Morin, 1950; Verwey, 1939), so these minerals can be excluded as contaminants. Goethite undergoes a characteristic SIRM decrease during warming from low temperatures (Dekkers, 1989b; Liu et al., 2006; Maher et al., 2004; Rochette & Fillion, 1989), which is consistent with the measured data and could reflect the presence of goethite impurities in these samples. Greigite has no low-temperature transition (e.g., Chang et al., 2009), so the SIRM warming curves in Figure 4c could also be due to greigite. These possibilities can be assessed with other low-temperature magnetic measurements.

LTC of RT-SIRM results for monoclinic pyrrhotite contain a Besnus transition below which cooling and warming curves are identical and above which they are distinct (Figure 4e), as observed by Rochette et al. (1990). Results for pyrrhotite-bearing nodules (Figure 4f) are again distinct from those for monoclinic pyrrhotite, where the curves are humped and have no indication of a Besnus transition. They have distinctly different forms to LTC-RT-SIRM curves for single-domain and multidomain greigite (Chang et al., 2009). LTC-RT-SIRM curves for goethite increase systematically from 300 to 5 K (Liu et al., 2006). Thus, known greigite and goethite impurities in the authigenic pyrrhotite-bearing nodules can be excluded as an explanation for the humped curves. Maghemitized magnetite produces humped curves (Chang et al., 2013; Özdemir & Dunlop, 2010), but such curves are different in detail to those observed here, so a contribution from maghemite can also be excluded. Thus, the LTC-RT-SIRM data for pyrrhotite-bearing nodules appear to be distinctive.

A range of environmentally abundant Fe oxyhydroxides (lepidocrocite, γ-FeOOH), Fe and Mn carbonates (siderite, $FeCO_3$; rhodochrosite, and $MnCO_3$), and Fe phosphates (vivianite, $Fe_3(PO_4)_2 \cdot 8H_2O$) occur as

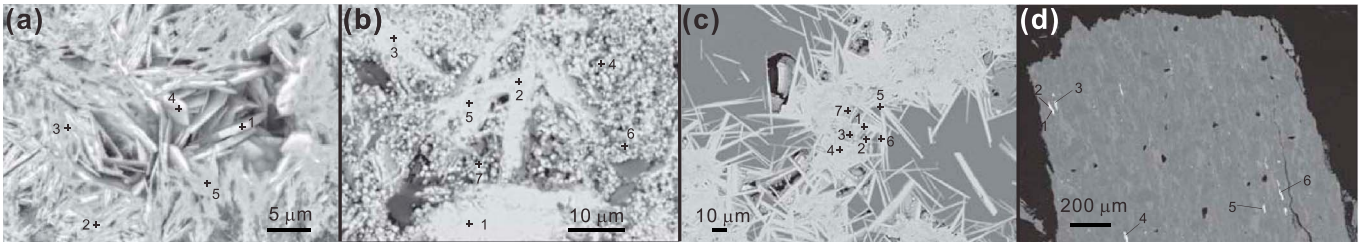

Figure 3. Electron back-scattered SEM images of the studied samples with spots indicated for EDS/WDS analyses where elemental abundance results and S/Fe ratios are listed in Table 2. (a) Nodule from a depth of 12.02 m in core MD10-3276 with five measurement spots indicated, (b) nodule from EJC site 29 with seven measurement spots indicated, (c) nodule from Valle Ricca, Rome, Italy, with seven measurement spots indicated, and (d) metamorphic pyrrhotite from site M11–131 with six measurement spots indicated. SEM = scanning electron microscope; EDS = energy dispersive spectrometer; WDS = wavelength dispersive X-ray spectrometers.

Table 2
Atomic Percentages and Fe/S Ratios for Analyzed Pyrrhotite-Bearing Samples

Sample	Spot location[a]	O	Al	Si	S	Fe	Cu	Ni	As	Total (%)	S/Fe[b]
MD10-3276 nodule	1	26.36			37.24	36.40				100.00	1.02
(Figure 3a)	2	39.86			28.05	32.09				100.00	0.87
	3	42.96			25.61	31.43				100.00	0.82
	4	40.28			27.56	32.18				100.02	0.86
	5	64.71			6.44	28.85				100.00	0.22
EJC29 nodule	1	1.52	0.06	0.48	52.78	44.30	0.23		0.63	100.00	1.19
(Figure 3b)	2	4.58	0.49	0.19	49.99	44.95			0.07	100.27	1.11
	3	5.14	0.13	0.79	50.08	44.07			0.34	100.55	1.14
	4	39.55	1.14	1.00	30.05	27.86	0.17		0.23	100.00	1.08
	5	3.69	0.27	0.78	52.19	43.47				100.40	1.20
	6	42.08	0.79	0.93	27.66	28.31	0.15		0.09	100.01	0.98
	7	10.61		0.60	48.77	39.81	0.48			100.27	1.23
Valle Rica nodule	1				53.43	46.57				100.00	1.15
(Figure 3c)	2				52.66	47.34				100.00	1.11
	3	45.71			35.58	17.81				99.10	1.90
	4	16.91			44.56	38.52				99.99	1.16
	5				54.43	45.57				100.00	1.19
	6				54.16	45.84				100.00	1.18
	7	17.61			47.10	35.29				100.00	1.33
Metamorphic	1				54.22	45.62		0.16	0.00	100.00	1.19
Pyrrhotite	2				53.10	46.72		0.18	0.00	100.00	1.14
(Figure 3d)	3				53.42	46.41		0.15	0.02	100.00	1.15
	4				53.59	46.25		0.14	0.03	100.01	1.16
	5				53.68	46.06		0.23	0.00	99.97	1.17
	6				53.91	45.88		0.18	0.04	100.01	1.18

[a]Spot locations for analyses of each sample are indicated in Figure 3. [b]Chemical compositions for selected authigenic and monoclinic pyrrhotite grains revealed from EDS analyses do not coincide precisely with the expected S/Fe values of 1.11 and 1.14, respectively, because the 10 μm electron beam diameter is larger than individual grains under analysis and because of surficial oxidation of iron sulfide minerals. Analyzed mineral surfaces may also be uneven and the polish quality of resin-impregnated sections can vary. Fe contributes to iron sulfide and (oxyhydr-)oxide minerals and O, Si, and Al contribute to matrix aluminosilicate minerals.

authigenic phases in diverse diagenetic environments. These minerals are paramagnetic at ambient temperatures, but they are magnetically ordered at low temperatures so they are worth considering in relation to the low-temperature magnetism of hexagonal (3T) pyrrhotite. The only one of these minerals that has been detected above the 0.1% level in our synchrotron XRD results is lepidocrocite (Figure 2), which become magnetically ordered below 50–70 K, and in which markedly higher SIRM values are observed below 30 K (Guyodo et al., 2016; Hirt et al., 2002; Lee et al., 2004). Similarly, higher magnetizations occur below 30–40 K for siderite (Frederichs et al., 2003; Housen et al., 1996), six-line ferrihydrite (Guyodo et al., 2006), rhodochrosite (Frederichs et al., 2003; Kosterov et al., 2006), and vivianite (Frederichs et al., 2003), and higher susceptibilities occur below 30 K for ankerite (Hilscher et al., 2005). As discussed by Kars et al. (2011) in relation to discriminating between monoclinic pyrrhotite and these other minerals based on low-temperature measurements, potential ambiguities can be resolved by use of a range of diagnostic magnetic analyses below 50 K. The key point in this context is that the large magnetization changes observed for these minerals below 50 K will only cause ambiguities with respect to monoclinic pyrrhotite (Figures 4a, 4e, and 5a) rather than authigenic hexagonal (3T) pyrrhotite, which does not undergo large magnetization changes below 50 K (Figures 4c, 4f, and 5b). We, thus, conclude that the potential mineralogical impurities considered here do not explain the observed low-temperature magnetic properties of authigenic hexagonal (3T) pyrrhotite.

Low-temperature B_c trends are also markedly different for monoclinic pyrrhotite compared to those for authigenic pyrrhotite-bearing nodules (Figures 4g and 4h). As observed by Rochette et al. (1990), a local B_c minimum occurs at ~30–34 K for all monoclinic pyrrhotite samples, followed by B_c increases with further cooling (Figure 4g). In some samples, B_c reaches a local maximum at ~20 K, and in others it continues to increase to larger values (~260–400 mT) than the >100 mT value observed below ~30–34 K by Rochette et al. (1990) for a large monocrystal. Increased B_c in monoclinic pyrrhotite below ~30–34 K is consistent with the suggestion of Rochette et al. (1990) that it is due to a change in the magnetization easy axis direction within the basal plane. This behavior contrasts with that of authigenic nodules that contain hexagonal (3T)

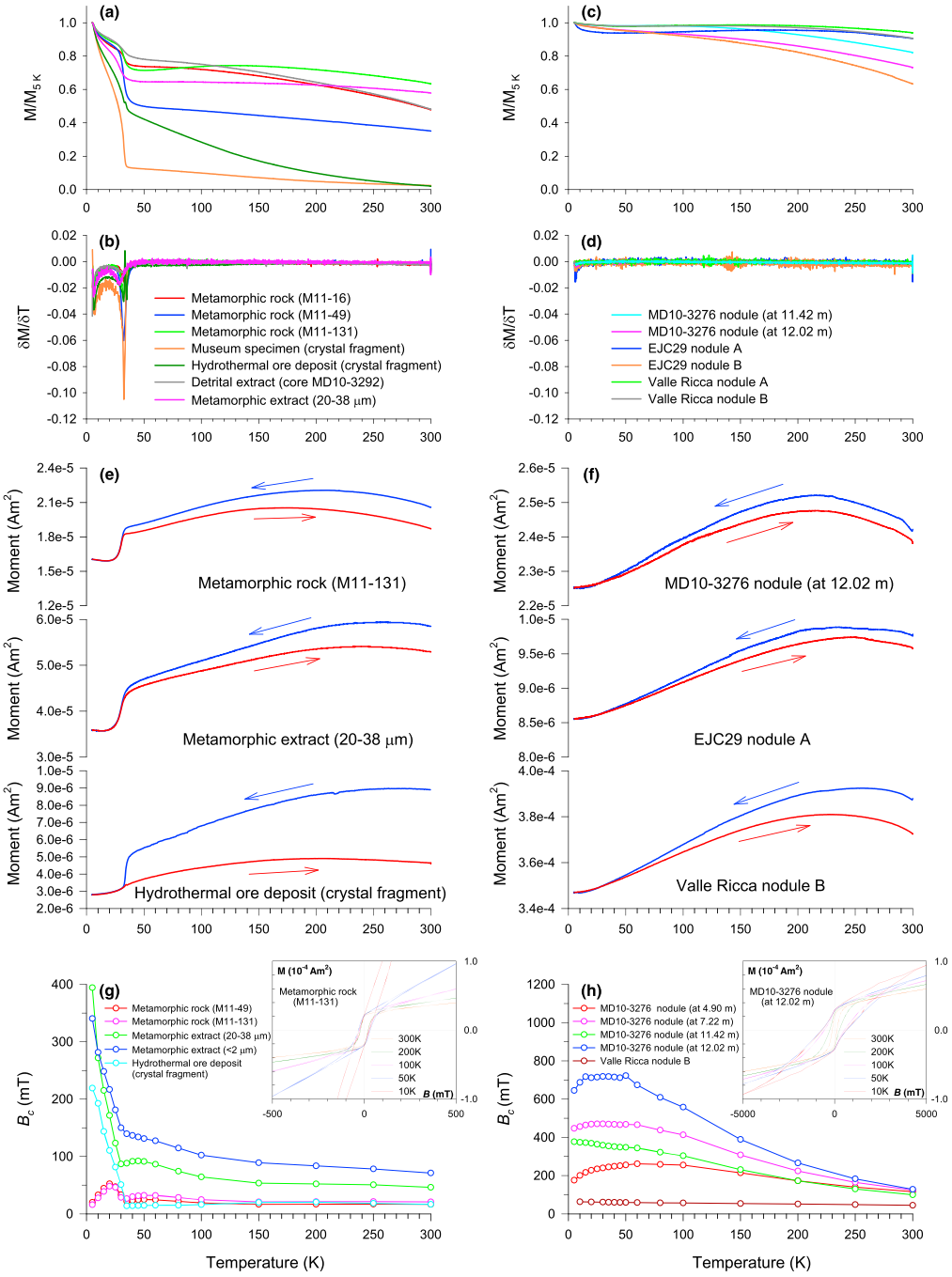

Figure 4. Low-temperature magnetic data for monoclinic and hexagonal pyrrhotite. (a) SIRM warming curves (normalized by the saturation isothermal remanent magnetization (SIRM) value at 5 K) for monoclinic pyrrhotite from the following: metamorphic bulk rock samples from the M11 section, Central Range, Taiwan, museum and hydrothermal samples, a magnetic extract from marine sediment core MD10-3292 (Figure 1d), and a magnetic extract from metamorphic rocks from the M11 section, Central Range, Taiwan (upper) with (b) first derivative of the curves indicating a sharp Besnus transition in all samples. (c) SIRM curves with (d) first derivatives for authigenic pyrrhotite-bearing nodules from indicated depths in core MD10-3276, the Erh-Jen Chi (EJC) section, southwestern Taiwan, and Valle Ricca, Italy. Low-temperature cycling of room temperature-SIRM results for selected (e) monoclinic pyrrhotite and (f) authigenic pyrrhotite-bearing samples. Representative B_c measurements from hysteresis loops (inset) at low temperatures for (g) monoclinic pyrrhotite and (h) authigenic pyrrhotite-bearing samples. Room temperature B_c values of authigenic pyrrhotite nodules are usually higher (100–130 mT) than those of monoclinic pyrrhotite samples (16–70 mT, depending on grain size), except for the Valle Ricca nodule that contains significant greigite impurities (Figure 2c).

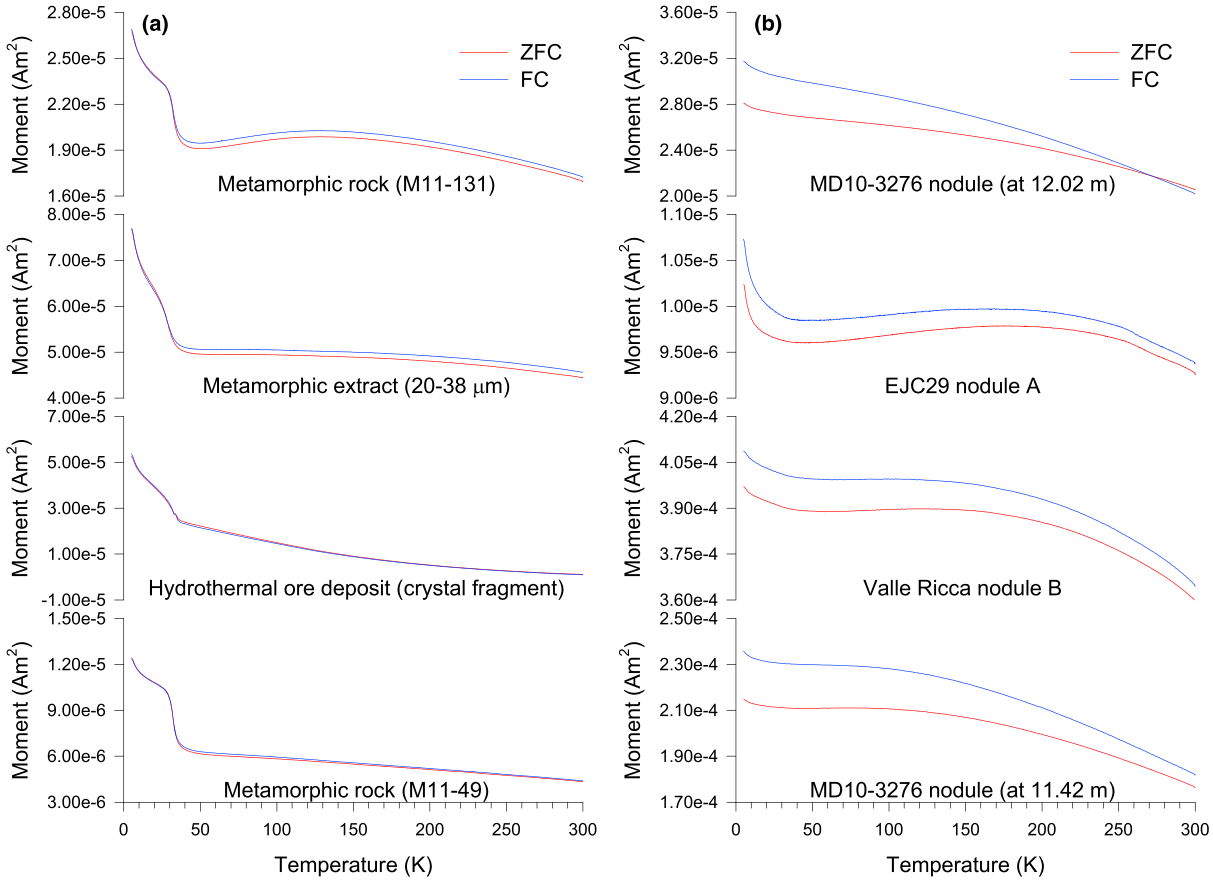

Figure 5. Zero-field-cooled/field-cooled magnetization curves for representative pyrrhotite samples. Results are for (a) monoclinic pyrrhotite and (b) authigenic hexagonal (3T) pyrrhotite. The samples are the same as in Figure 4. Zero-field-cooled curves are red and field-cooled curves are blue.

pyrrhotite, which have high B_c values at all temperatures, including room temperature, and which generally increase with decreasing temperature to plateau at 10–50 K. Maximum observed B_c values exceed 700 mT, which are underestimates because the hysteresis loops in question are not saturated even in applied fields of 5 T (Figure 4h, inset). Such exceptionally high coercivities have not been observed previously for pyrrhotite at low temperatures. They further indicate the distinctiveness of the low-temperature magnetic properties documented here for hexagonal (3T) pyrrhotite even though they lack a Besnus transition signature.

4. Discussion

Authigenic pyrrhotite-bearing nodules have magnetic remanence-bearing properties at room temperature and at low temperatures, with no Besnus transition, humped LTC-RT-SIRM curves without inflection at ~34 K and exceptionally high coercivities in some samples (>700 mT) with maxima at ~15–50 K (Figures 4c, 4d, 4f, and 4h). The distinctiveness of these magnetic properties leads us to suggest that they are due to hexagonal (3T) pyrrhotite. The observed low-temperature magnetic properties in hexagonal (3T) pyrrhotite cannot be explained either by known contaminants (e.g., goethite, greigite, and lepidocrocite) or by undetected contaminants (e.g., magnetite, maghemite, and hematite) that, if present, must only occur in concentrations <0.1% based on synchrotron XRD results (Figures 2a–2c). Furthermore, these minerals are not indicated by their own distinctive low-temperature magnetic properties. The authigenic nodules are macroscopically magnetic and are attracted by a rare-earth magnet, which is also unlikely to be due to a <0.1% impurity. The presence of a measurable magnetization and coercivity at all temperatures from 5 to 300 K (Figures 4f and 4h) contrasts with the expectation that hexagonal pyrrhotite has an

Table 3
Magnetic Parameters for the Studied Samples

Sample	Mass (10^{-6} kg)	Initial slope (Am^2/T)	χ from initial slope (m^3/kg)	M_{rs} (Am^2/kg)	M_s (Am^2/kg)	B_{cr} (mT)	B_c (mT)	M_{rs}/M_s	B_{cr}/B_c
MD10-3276 7.22 m nodule	44.2	2.85×10^{-4}	8.10×10^{-6}	2.36	3.43	154.6	123.1	0.69	1.26
EJC29 nodule A	19.9			0.47	0.83	82.8	62.3	0.56	1.33
EJC29 nodule B	4.7			4.03	6.81	77.1	58.9	0.59	1.31
EJC29 nodule C	4.4	4.43×10^{-5}	1.27×10^{-5}	1.18	1.94	82.9	61.2	0.61	1.36
EJC29 nodule D	2.9			4.52	7.83	75.3	56.9	0.58	1.32
EJC29 nodule E	2.0			3.68	6.31	75.2	58.0	0.58	1.30
EJC29 nodules	17.8	5.25×10^{-4}	3.72×10^{-5}	2.83	4.76	86.7	59.7	0.60	1.45
Valle Ricca nodule A	36.6			9.06	18.17	65.2	46.4	0.50	1.40
Valle Ricca nodule B	94.1			1.44	3.27	55.9	37.5	0.44	1.49
Valle Ricca nodule C	76.9			8.09	18.76	65.9	43.0	0.43	1.53
Valle Ricca nodule D	44.9	4.99×10^{-3}	1.40×10^{-4}	10.18	18.37	58.0	43.6	0.55	1.33
Valle Ricca nodule E	233.8	3.34×10^{-2}	1.79×10^{-4}	10.94	25.10	63.7	42.5	0.44	1.50
M11–131 bulk[a]	491.3	3.92×10^{-4}	1.00×10^{-6}	0.04	0.08	30.9	26.7	0.56	1.16

[a]The concentration of monoclinic pyrrhotite in this bulk phyllite sample is extremely low, so concentration-dependent magnetic parameters (χ, M_{rs}, and M_s) are correspondingly low.

antiferromagnetic structure. We, therefore, propose tentatively that the 3T pyrrhotite polytype has previously unrecognized ferrimagnetic properties as discussed below.

Bulk magnetic parameters for the studied pyrrhotite samples are presented in Table 3. M_{rs} and M_s are variable because of variable concentrations of pyrrhotite and impurities in the samples; correction based on their estimated concentrations reported in Table 1 would be imprecise, so we have not attempted to do so. For example, the Valle Ricca nodules contain significant greigite concentrations, where greigite has a room temperature M_s value of ~67 A m^2/kg (Li et al., 2014), which undoubtedly contributes to the high M_s values of these samples. Nevertheless, greigite is absent from the other studied samples (Table 1) and the lack of strongly magnetic impurities indicates M_s values of the order of several A m^2/kg. Such values are likely to reflect genuine ferrimagnetic behavior rather than canted antiferromagnetism or defect magnetism in an antiferromagnetic material. For example, variable contributions from the latter two magnetization types give rise to variable M_s values in hematite that range between 0.2 and 0.5 A m^2/kg (e.g., de Boer & Dekkers, 1998; Dunlop, 1971; O'Reilly, 1984). These values are about a factor of 10 lower than those reported in Table 3, which represent underestimates of their true M_s value because the samples contain other minerals in addition to hexagonal (3T) pyrrhotite (Table 1).

Confirmation of a room temperature ferrimagnetism in hexagonal (3T) pyrrhotite awaits neutron diffraction or Mössbauer analysis to determine the sublattice magnetizations to understand any potential deviation from the expected antiferromagnetic structure. Future detailed work of this type is beyond the scope of the present study but is planned to enable more complete explanation of the hypothesized magnetism. Regardless, the low-temperature magnetic properties contrast strongly with those of monoclinic pyrrhotite for which a clear Besnus transition signature is always observed in our samples (Figures 4a, 4b, 4e, and 5a). The origin of the high coercivities of hexagonal (3T) pyrrhotite at ~15–50 K requires explanation; these high coercivities are not related obviously to a Besnus-type transition, but they suggest a change in magnetic structure or anisotropy arrangement at low temperatures.

While our work raises several unanswered questions that require further investigation, the results presented here are important for understanding magnetic signatures associated with active or fossil gas hydrates and methane venting. Importantly, remanence-bearing pyrrhotite has been documented widely in such settings but has been assumed to be monoclinic rather than hexagonal (e.g., Kars & Kodama, 2015; Larrasoaña et al., 2007; Roberts, 2015; Weaver et al., 2002), because the former is known to be ferrimagnetic whereas the latter is assumed to be antiferromagnetic. Our work demonstrates that nodular authigenic pyrrhotite, which is identified routinely in sites with active or fossil gas hydrate/methane venting, is of the hexagonal (3T) rather than the monoclinic (4M) variety. Observed magnetism in hexagonal (3T) pyrrhotite indicates that care is needed when interpreting environmental and magnetic signals from such environments. Further work is needed to provide a clearer explanation of the magnetic properties of hexagonal (3T) pyrrhotite as documented here.

5. Conclusions

We observe consistently a clear Besnus transition signature in monoclinic (4M) pyrrhotite that is not observed in hexagonal (3T) pyrrhotite. The lack of a low-temperature transition would not be surprising if 3T pyrrhotite is antiferromagnetic at all temperatures, but the presence of a magnetic remanence that cannot be due to known and potentially unidentified impurities leads us to propose that the studied 3T pyrrhotite is ferrimagnetic and capable of carrying a remanence from 5 K to 300 K. The hexagonal (3T) pyrrhotite has high coercivities at room temperature (~100–130 mT in our samples from active gas hydrate settings) and higher coercivities (up to >700 mT) at ~15–50 K. The unexpected nature of our results and the lack of detailed studies of the magnetic properties of 3T pyrrhotite suggests that further detailed magnetic and crystallographic studies are needed to develop a more complete understanding of this mineral, which occurs widely in active or fossil gas hydrate/methane venting environments.

Acknowledgments

We are grateful to Kuo-Hang Chen and Chun-Hung Lin for assistance with laboratory work, the National Synchrotron Radiation Research Center, Taiwan, for XRD analyses, Yoshiyuki Iizuka for assistance with microprobe analyses, an anonymous reviewer and Bernie Housen for constructively helpful reviews that improved the paper, and Ulrich Faul for editorial handling. Kung-Suan Ho and Wei-Teh Jiang kindly supplied monoclinic pyrrhotite crystals from museum and ore mineral collections, respectively. C. S. H. acknowledges funding from the Central Geological Survey and Ministry of Science and Technology, R.O.C., through grants 104-5226904000-02-01 and MOST 105-2116-M-001-018, respectively. A. P. R. acknowledges funding from the Australian Research Council through grant DP160100805. Data presented in this paper are available at http://dmc.earth.sinica.edu.tw/Contributor/Horng/2018mag-1.

References

Arnold, R. G. (1966). Mixtures of hexagonal and monoclinic pyrrhotite and the measurement of the metal content of pyrrhotite by X-ray diffraction. *American Mineralogist*, *51*, 1221–1227.

Batt, A. P. (1972). Nickel distribution in hexagonal and monoclinic pyrrhotite. *Canadian Mineralogist*, *11*, 892–897.

Bennett, C. E. G., & Graham, J. (1981). New observations on natural pyrrhotites: Magnetic transition in hexagonal pyrrhotite. *American Mineralogist*, *66*, 1254–1257.

Besnus, M. J., & Meyer, A. J. (1964). Nouvelles données expérimentales sur le magnétisme de la pyrrhotine naturelle. Paper Presented at Proceedings of the International Conference on Magnetism, Nottingham, England, 507–511.

Chang, L., Roberts, A. P., Rowan, C. J., Tang, Y., Pruner, P., Chen, Q., & Horng, C.-S. (2009). Low-temperature magnetic properties of greigite (Fe_3S_4). *Geochemistry, Geophysics, Geosystems*, *10*, Q01Y04. https://doi.org/10.1029/2008GC002276

Chang, L., Winklhofer, M., Roberts, A. P., Heslop, D., Florindo, F., Dekkers, M. J., et al. (2013). Low-temperature magnetic properties of pelagic carbonates: Oxidation of biogenic magnetite and identification of magnetosome chains. *Journal of Geophysical Research: Solid Earth*, *118*, 6049–6065. https://doi.org/10.1002/2013JB010381

Clark, L. A. (1960). The Fe-As-S system: Phase relations and applications. *Economic Geology*, *55*(7), 1345–1381. https://doi.org/10.2113/gsecongeo.55.7.1345

de Boer, C. B., & Dekkers, M. J. (1998). Thermomagnetic behaviour of haematite and goethite as a function of grain size in various non-saturating magnetic fields. *Geophysical Journal International*, *133*(3), 541–552. https://doi.org/10.1046/j.1365-246X.1998.00522.x

Dekkers, M. J. (1989a). Magnetic properties of natural pyrrhotite. II. High- and low-temperature behaviour of J_{rs} and TRM as function of grain size. *Physics of the Earth and Planetary Interiors*, *57*(3-4), 266–283. https://doi.org/10.1016/0031-9201(89)90116-7

Dekkers, M. J. (1989b). Magnetic properties of natural goethite–II. TRM behaviour during thermal and alternating field demagnetization and low-temperature treatment. *Geophysical Journal*, *97*(2), 341–355. https://doi.org/10.1111/j.1365-246X.1989.tb00505.x

Dekkers, M. J., Mattéi, J.-L., Fillion, G., & Rochette, P. (1989). Grain-size dependence of magnetic behavior of pyrrhotite during its low temperature transition at 34 K. *Geophysical Research Letters*, *16*, 855–858. https://doi.org/10.1029/GL016i008p00855

Dunlop, D. J. (1971). Magnetic properties of fine-particle hematite. *Annales de Géophysique*, *27*, 269–293.

Fillion, G., & Rochette, P. (1988). The low temperature transition in monoclinic pyrrhotite. *Journal de Physique, Colloque*, *49*, C8-907–C8-908. https://doi.org/10.1051/jphyscol:19888412

Fleet, M. E. (1971). The crystal structure of a pyrrhotite (Fe_7S_8). *Acta Crystallographica*, *B27*, 1864–1867. https://doi.org/10.1107/S0567740871004990

Florindo, F., & Sagnotti, L. (1995). Palaeomagnetism and rock magnetism at the upper Pliocene Valle Ricca (Rome, Italy) section. *Geophysical Journal International*, *123*(2), 340–354. https://doi.org/10.1111/j.1365-246X.1995.tb06858.x

Frederichs, T., von Dobeneck, T., Bleil, U., & Dekkers, M. J. (2003). Towards the identification of siderite, rhodochrosite, and vivianite in sediments by their low-temperature magnetic properties. *Physics and Chemistry of the Earth*, *28*(16-19), 669–679. https://doi.org/10.1016/S1474-7065(03)00121-9

Graham, A. R. (1969). Quantitative determination of hexagonal and monoclinic pyrrhotites by X-ray diffraction. *Canadian Mineralogist*, *10*, 4–24.

Guyodo, Y., Banerjee, S. K., Penn, R. L., Burleson, D., Berquo, T., Seda, T., & Solheid, P. (2006). Magnetic properties of synthetic six-line ferrihydrite nanoparticles. *Physics of the Earth and Planetary Interiors*, *154*(3-4), 222–233. https://doi.org/10.1016/j.pepi.2005.05.009

Guyodo, Y., Bonville, P., Till, J. L., Ona-Nguema, G., Lagroix, F., & Menguy, N. (2016). Constraining the origins of the magnetism of lepidocrocite (γ-FeOOH): A Mössbauer and magnetization study. *Frontiers in Earth Science*, *4*, 28. https://doi.org/10.3389/feart. 2016.00028

Han, J. T., & Fyfe, W. S. (2000). Arsenic removal from water by iron-sulphide minerals. *Chinese Science Bulletin*, *45*(15), 1430–1434. https://doi.org/10.1007/BF02886253

Hilscher, G., Rogl, P., Zemann, J., & Ntaflos, T. (2005). Low-temperature magnetic investigation of ankerite. *European Journal of Mineralogy*, *17*(1), 103–106. https://doi.org/10.1127/0935-1221/2005/0017-0103

Hirt, A. M., Lanci, L., Dobson, J., Weidler, P., & Gehring, A. U. (2002). Low-temperature magnetic properties of lepidocrocite. *Journal of Geophysical Research*, *107*(B1), 2011. https://doi.org/10.1029/2001JB000242

Hoffmann, V., Stanjek, H., & Murad, E. (1993). Mineralogical, magnetic and Mössbauer data of smythite (Fe_9S_{11}). *Studia Geophysica et Geodaetica*, *37*(4), 366–381. https://doi.org/10.1007/BF01613583

Horng, C.-S. (2018). Unusual magnetic properties of sedimentary pyrrhotite in methane seepage sediments: Comparison with metamorphic pyrrhotite and sedimentary greigite. *Journal of Geophysical Research: Solid Earth*, 123. https://doi.org/10.1002/2017JB015262

Horng, C.-S., Huh, C.-A., Chen, K.-H., Lin, C.-H., Shea, K.-S., & Hsiung, K.-H. (2012). Pyrrhotite as a tracer for denudation of the Taiwan orogen. *Geochemistry, Geophysics, Geosystems*, *13*, Q08Z47. https://doi.org/10.1029/2012GC004195

Horng, C.-S., & Roberts, A. P. (2006). Authigenic or detrital origin of pyrrhotite in sediments?: Resolving a paleomagnetic conundrum. *Earth and Planetary Science Letters*, *241*(3-4), 750–762. https://doi.org/10.1016/j.epsl.2005.11.008

Housen, B. A., Banerjee, S. K., & Moskowitz, B. M. (1996). Low-temperature magnetic properties of siderite and magnetite in marine sediments. *Geophysical Research Letters*, *23*(20), 2843–2846.

Jiang, W.-T., Horng, C.-S., Roberts, A. P., & Peacor, D. R. (2001). Contradictory magnetic polarities in sediments and variable timing of neoformation of authigenic greigite. *Earth and Planetary Science Letters*, *193*, 1–12. https://doi.org/10.1016/S0012-821X(01)00497-6,1-2

Kars, M., Aubourg, C., & Pozzi, J.-P. (2011). Low temperature magnetic behavior near 35 K in unmetamorphosed claystones. *Geophysical Journal International*, *186*(3), 1029–1035. https://doi.org/10.1111/j.1365-246X.2011.05121.x

Kars, M., & Kodama, K. (2015). Authigenesis of magnetic minerals in gas hydrate-bearing sediments in the Nankai trough, offshore Japan. *Geochemistry, Geophysics, Geosystems*, *16*, 947–961. https://doi.org/10.1002/2014GC005614

Kosterov, A., Frederichs, T., & von Dobeneck, T. (2006). Low-temperature magnetic properties of rhodochrosite ($MnCO_3$). *Physics of the Earth and Planetary Interiors*, *154*(3-4), 234–242. https://doi.org/10.1016/j.pepi.2005.09.011

Koulialias, D., Kind, J., Charilaou, M., Weidler, P. G., Löffler, J. F., & Gehring, A. U. (2016). Variable defect structures cause the magnetic low-temperature transition in natural monoclinic pyrrhotite. *Geophysical Journal International*, *204*(2), 961–967. https://doi.org/10.1093/gji/ggv498

Larrasoaña, J. C., Roberts, A. P., Musgrave, R. J., Gràcia, E., Piñero, E., Vega, M., & Martínez-Ruiz, F. (2007). Diagenetic formation of greigite and pyrrhotite in gas hydrate marine sedimentary systems. *Earth and Planetary Science Letters*, *261*(3-4), 350–366. https://doi.org/10.1016/j.epsl.2007.06.032

Lee, G. H., Kim, S. H., Choi, B. J., Huh, S. H., Chang, Y., Kim, B., et al. (2004). Magnetic properties of needle-like γ-FeOOH and γ-FeOOH nanoparticles. *Journal of the Korean Physical Society*, *45*, 1019–1024.

Li, G. W., Zhang, B. M., Yu, F., Novakova, A. A., Krivenkov, M. S., Kiseleva, T. Y., et al. (2014). High-purity Fe_3S_4 greigite microcrystals for magnetic and electrochemical performance. *Chemistry of Materials*, *26*(20), 5821–5829. https://doi.org/10.1021/cm501493m

Liu, Q., Yu, Y. J., Torrent, J., Roberts, A. P., Pan, Y., & Zhu, R. (2006). Characteristic low-temperature magnetic properties of aluminous goethite [α-(Fe, Al)OOH] explained. *Journal of Geophysical Research*, *111*, B12S34. https://doi.org/10.1029/2006JB004560

Maher, B. A., Karloulovski, V. V., & Mutch, T. J. (2004). High-field remanence properties of synthetic and natural submicrometre haematites and goethites: Significance for environmental contexts. *Earth and Planetary Science Letters*, *226*(3-4), 491–505. https://doi.org/10.1016/j.epsl.2004.05.042

Mineral Powder Diffraction File Databook, Sets 1–42, (1993). Published by International Centre for Diffraction Data (ICDD), Swarthmore, Pennsylvania, U.S.A.

Morimoto, N., Gyobu, A., Mukaiyama, H., & Izawa, E. (1975). Crystallography and stability of pyrrhotites. *Economic Geology*, *70*, 824–833. https://doi.org/10.2113/gsecongeo.70.4.824

Morin, F. J. (1950). Magnetic susceptibility of αFe_2O_3 and αFe_2O_3 with added titanium. *Physical Review*, *78*(6), 819–820. https://doi.org/10.1103/PhysRev.78.819.2

O'Reilly, W. (1984). *Rock and mineral magnetism* (p. 220). Glasgow: Blackie and Son. https://doi.org/10.1007/978-1-4684-8468-7

O'Reilly, W., Hoffman, V., Chouker, A. C., Soffel, H. C., & Menyeh, A. (2000). Magnetic properties of synthetic analogues of pyrrhotite ore in the grain size range 1–24 μm. *Geophysical Journal International*, *142*(3), 669–683. https://doi.org/10.1046/j.1365-246x.2000.00169.x

Özdemir, Ö., & Dunlop, D. J. (2010). Hallmarks of maghemitization in low-temperature remanence cycling of partially oxidized magnetite nanoparticles. *Journal of Geophysical Research*, *115*, B02101. https://doi.org/10.1029/2009JB006756

Pósfai, M., Sharp, T., & Kontny, A. (2000). Pyrrhotite varieties from the 9.1 km deep borehole of the KTB project. *American Mineralogist*, *85*(10), 1406–1415. https://doi.org/10.2138/am-2000-1009

Powell, A. V., Vaqueiro, P., Knight, K. S., Chapon, L. C., & Sánchez, R. D. (2004). Structure and magnetism in synthetic pyrrhotite Fe_7S_8: A powder neutron-diffraction study. *Physical Review, B*, *70*(1). https://doi.org/10.1103/PhysRevB.70.014415

Rietveld, H. M. (1969). A profile refinement method for nuclear and magnetic structures. *Journal of Applied Crystallography*, *2*(2), 65–71. https://doi.org/10.1107/S0021889869006558

Roberts, A. P. (2015). Magnetic mineral diagenesis. *Earth-Science Reviews*, *151*, 1–47. https://doi.org/10.1016/j.earscirev.2015.09.010

Roberts, A. P., Chang, L., Rowan, C. J., Horng, C. S., & Florindo, F. (2011). Magnetic properties of sedimentary greigite (Fe_3S_4): An update. *Reviews of Geophysics*, *49*, RG1002. https://doi.org/10.1029/2010RG000336

Rochette, P. (1987). Metamorphic control of the magnetic mineralogy of black shales in the Swiss Alps: Toward the use of magnetic isograds. *Earth and Planetary Science Letters*, *84*, 446–456. https://doi.org/10.1016/0012-821X(87)90009-4

Rochette, P., & Fillion, G. (1989). Field and temperature behavior of remanence in synthetic goethite: Paleomagnetic implications. *Geophysical Research Letters*, *16*, 851–854. https://doi.org/10.1029/GL016i008p00851

Rochette, P., Fillion, G., Mattéi, J.-L., & Dekkers, M. J. (1990). Magnetic transition at 30–34 K in Fe_7S_8: Insight into a widespread occurrence of pyrrhotite in rocks. *Earth and Planetary Science Letters*, *98*(3-4), 319–328. https://doi.org/10.1016/0012-821X(90)90034-U

Rochette, P., Gattacceca, J., Chevrier, V., Hoffmann, V., Lorand, J.-P., Funaki, M., & Hochleitner, R. (2005). Matching Martian crustal magnetization and magnetic properties of Martian meteorites. *Meteoritics and Planetary Science*, *40*(4), 529–540. https://doi.org/10.1111/j.1945-5100.2005.tb00961.x

Schwarz, E. J. (1975). Magnetic properties of pyrrhotite and their use in applied geology and geophysics. *Geological Survey of Canada Paper*, 74–59.

van Dongen, B. E., Roberts, A. P., Schouten, S., Jiang, W.-T., Florindo, F., & Pancost, R. D. (2007). Formation of iron sulfide nodules during anaerobic oxidation of methane. *Geochimica et Cosmochimica Acta*, *71*, 5155–5167. https://doi.org/10.1016/j.gca.2007.08.019,21

Verwey, E. J. W. (1939). Electronic conduction of magnetite (Fe_3O_4) and its transition point at low temperatures. *Nature*, *144*(3642), 327–328. https://doi.org/10.1038/144327b0

Volk, M. W. R., Gilder, S. A., & Feinberg, J. M. (2016). Low-temperature magnetic properties of monoclinic pyrrhotite with particular reference to the Besnus transition. *Geophysical Journal International*, *207*(3), 1783–1795. https://doi.org/10.1093/gji/ggw376

Walz, F. (2002). The Verwey transition—A topical review. *Journal of Physics: Condensed Matter*, *14*, R285–R340. http://stacks.iop.org/cm/14/R285

Weaver, R., Roberts, A. P., & Barker, A. J. (2002). A late diagenetic (syn-folding) magnetization carried by pyrrhotite: Implications for paleomagnetic studies from magnetic iron sulphide-bearing sediments. *Earth and Planetary Science Letters*, *200*, 371–386. https://doi.org/10.1016/S0012-821X(02)00652-0,3-4

Wolfers, P., Fillion, G., Ouladdiaf, B., Ballou, R., & Rochette, P. (2011). The pyrrhotite 32K magnetic transition. *Solid State Phenomena*, *170*, 174–179. https://doi.org/10.4028/www.scientific.net/SSP.170.174